Scatterometer and Model Wind and Wind Stress in the Oregon–Northern California Coastal Zone

N. PERLIN, R. M. SAMELSON, AND D. B. CHELTON

College of Oceanic and Atmospheric Sciences, Oregon State University, Corvallis, Oregon

ABSTRACT

Measurements of surface wind stress by the SeaWinds scatterometer on NASA's Quick Scatterometer (QuikSCAT) satellite are analyzed and compared with several different atmospheric model products, from an operational model and two high-resolution nested regional models, during two summer periods, June through September 2000 and 2001, in the coastal region west of Oregon and northern California. The mean summer wind stress had a southward component over the entire region in both years. Orographic intensifications of both the mean and fluctuating wind stress occurred near Cape Blanco, Cape Mendocino, and Point Arena. Substantial differences between the model products are found for the mean, variable, and diurnal wind stress fields. Temporal correlations with the QuikSCAT observations are highest for the operational model, and are not improved by either nested model. The highest-resolution nested model most accurately reproduced the mean observed stress fields, but slightly degrades the temporal correlations due to incoherent high-frequency (0.5–2 cpd) fluctuations. The QuikSCAT data reveal surprisingly strong diurnal fluctuations that extend offshore 150 km or more with magnitudes that are a significant fraction of the mean wind stress. Wind stress curl fields from QuikSCAT and the models show local cyclonic and anticyclonic maxima associated with the orographic wind intensification around the capes. The present results are consistent with the hypothesis of a wind-driven mechanism for coastal jet separation and cold water plume and anticyclonic eddy formation in the California Current System south of Cape Blanco.

1. Introduction

Many different physical processes influence the structure of the lower atmosphere in the coastal zone, including its interactions with the land and sea surfaces. Coastal wind fields may have complex spatial structure, arising, for example, from orographic interactions. In addition to their meteorological interest and importance, coastal winds are an important driving force for coastal ocean circulation, especially in coastal upwelling regions such as the northwest coast of the United States. The present study is motivated by an interest in understanding and quantifying this influence of wind stress on ocean circulation along the U.S. West Coast.

Numerous observational and modeling studies have previously investigated the lower-tropospheric wind regime along the Oregon and California coastal zone (Elliott and O'Brien 1977; Zemba and Friehe 1987; Beardsley et al. 1987; Bakun and Nelson 1991; Samelson 1992; Samelson and Lentz 1994; Holt 1996; Burk and Thompson 1996; Bielli et al. 2002; Samelson et al. 2002). During the summertime, the flow along the coast is pre-dominantly northerly. A low-level jet (LLJ) is frequently found near or within the inversion that caps the moist, cool marine boundary layer. While the LLJ is forced primarily by the thermal wind resulting from sea–land differential heating, its meso-β-scale structure depends on the configuration of the local coastline and capes, and on coastal orography.

In the past, the data available for observational studies over the open ocean regions have typically been limited to sparse buoy or ship measurements, supplemented by occasional aircraft studies. Satellite scatterometry has provided for the first time the capability to make routine, daily measurements of the surface wind stress field on extended spatial and temporal scales, under most weather conditions (Naderi et al. 1991; Freilich and Dunbar 1999). High-resolution regional atmospheric modeling has also progressed, in part due to advances in computing technology, and now offers another useful tool for the study of the coastal lower atmosphere (e.g., Koračin and Dorman 2001: Bielli et al. 2002). Our purpose in this study is to compare scatterometer and model estimates of wind and wind stress over the coastal ocean in order to improve understanding of the coastal wind fields that drive coastal ocean circulation, and of the physical processes that control the structure of the coastal wind fields.

Corresponding author address: N. Perlin, College of Oceanic and Atmospheric Sciences, Oregon State University, 104 COAS Admin. Bldg., Corvallis, OR 97331-5503.
E-mail: nperlin@coas.oregonstate.edu

The scatterometer data used in the present study were obtained from the SeaWinds instrument on board the National Aeronautics and Space Administration (NASA) Quick Scatterometer (QuikSCAT) satellite. The model products used in the study were obtained from three different mesoscale models: the medium-resolution National Center for Environmental Prediction (NCEP) atmospheric Eta Model, and two high-resolution, meso-β-scale, nested regional models implemented locally. The study area extends from 35° to 49°N, and from the Oregon–California coast westward to 130°W. The domains for the two high-resolution models are centered at Newport (44.7°N, 124°W) on the Oregon coast, and are approximately 600 km on each side. The periods considered are June through September of 2000 and 2001, corresponding to the main climatological upwelling regime (Bakun and Nelson 1991).

Section 2 of the paper contains general information and descriptions of the QuikSCAT scatterometer data, as well as of the model products used in the study. Section 3 contains a discussion of the wind and wind stress fields in the full domain, available for QuikSCAT and the Eta Model; section 4 focuses on a smaller region near Cape Blanco, along the southern Oregon coast, and analyzes the wind stresses from QuikSCAT and all three models. Section 5 contains a discussion of the diurnal cycle, section 6 examines the empirical orthogonal functions (EOFs), section 7 discusses the wind stress curl fields and winds over the continental shelf, and section 8 contains a summary.

2. Data and model products

a. Satellite scatterometer

Data for this study were obtained from the SeaWinds scatterometer on board the QuikSCAT satellite (Liu 2002; Liu and Xie 2001) during two summer upwelling seasons, 20 June–30 September 2000, and 1 June–30 September 2001. The SeaWinds scatterometer is a scanning microwave radar that infers the surface wind stress from measurements of radar backscatter from the roughness of the sea surface at multiple antenna look angles (Naderi et al. 1991). The geophysical product of the scatterometer is the equivalent neutral stability wind vector interpolated onto a 0.25° output grid ($\approx$25 km). The equivalent neutral stability wind is the wind that would exist for a given wind stress if the atmospheric boundary layer were neutrally stratified, and is computed for QuikSCAT using the Large and Pond (1982) neutral stability drag coefficient. Wind stress is obtained here from QuikSCAT winds using the same Large and Pond (1982) neutral stability drag coefficient, effectively inverting the relation between wind and stress that is used in the calibration of the QuikSCAT wind retrievals. The accuracy of the QuikSCAT wind retrievals has been estimated to be $\approx$1.3 m s^{-1} in speed and

$\approx$19° in direction (Chelton and Freilich 2004, manuscript submitted to *Mon. Wea. Rev.*).

The study area extends from the Oregon–California coast offshore to 130°W, and 35°–49°N. In this area, the QuikSCAT orbit provides twice-daily coverage, nominally at 0300 UTC (ascending path) and 1400 UTC (descending), with timing variations up to approximately ±1 h. These correspond to local times of 2000 and 0700 PDT, respectively. To form a common period for the QuikSCAT and model time series, fields were excluded at times when simultaneous QuikSCAT and model output were not available. The missing dates in the year 2000 were 13, 14, 18, 22, 24, 25 July, 29 August, 2, 14, 24, 25 September. In June–September 2001 the only missing dates were in the satellite data on 7–8 July. There is a gap in the scatterometer measurements within about 30 km of the coast because of land contamination in the radar antenna sidelobes. Depending on the precise location of the radar backscatter measurements used in the vector wind retrievals, wind estimates are sometimes not available near the edge of this gap. The implications of this on the comparison of model and scatterometer stress fields are discussed in section 3b.

b. Regional atmospheric models

Surface fields from the operational NCEP 32-km hydrostatic Eta Model were obtained for this study from the standard 40-km output grid (# 212). Descriptions of the Eta Model physics, grid, and implementation can be found in Black (1994), Janjić (1994), Staudenmaier (1996), and Mittelstadt (1998) (see also http://www.comet.ucar.edu/nwplessons/etalesson2/index.htm). Daily Eta forecasts were initialized at 0000 UTC, and also included data assimilation. The planetary boundary layer (PBL) parameterization was based on the modified Mellor–Yamada level 2.5 scheme (Black 1994), in which the turbulent kinetic energy (TKE) is a prognostic variable, that is used to derive the transfer coefficients for momentum, heat, and moisture, and surface fluxes are computed using stability-corrected bulk formulas (Lobocki 1993). The model output was archived every 3 h, from which the forecasts for 0300 and 1500 UTC from each day were spliced together to form a continuous series of twice-daily fields that could be compared to the QuikSCAT data record. The Eta wind stress used here is the air–sea momentum flux computed by the PBL surface flux scheme.

In addition to the Eta output, model wind fields were obtained from high-resolution configurations of two mesoscale atmospheric models, the Coupled Ocean–Atmosphere Mesoscale Prediction System (COAMPS) of the Naval Research Laboratory, and Advanced Regional Prediction System (ARPS) of the University of Oklahoma. We implemented these models in a daily forecast mode, and surface output from the high-resolution inner nests of both models was archived hourly.

COAMPS is a three-dimensional mesoscale prediction system, designed for both idealized and real data simulations. The atmospheric part of the model system used in the present study is based on nonhydrostatic compressible dynamics, with explicit treatment of moist physics, and convective parameterizations. The vertical model grid utilizes a terrain-following (sigma-z) vertical coordinate. The model also allows for multiple nesting runs. A complete description of the model is given by Hodur (1997). The horizontal grid cells of the triply nested configuration had sizes 81, 27, and 9 km, respectively, all centered on 44.7°N, 124.0°W (Newport, Oregon). The vertical grid had 30 levels from the surface to approximately 31 km, with the first model level at 10 m above the ground. Simulations were started daily at 0000 UTC (cold start), with initial and boundary conditions from the Navy Operational Global Atmospheric Prediction System (NOGAPS), and no additional data assimilation ("cold start"). Only the results from the inner nest (9-km grid boxes) were analyzed in the present study. The 1.5-order closure, level 2.5 turbulence scheme of Mellor and Yamada (1982) was used in the boundary layer parameterization. A stability-corrected surface scheme following Louis (1979) and roughness length formulation following Fairall et al. (1996), were used to compute surface fluxes, including the surface wind stress.

For comparison with the twice-daily scatterometer observations, 3-h block averages of the archived hourly modeled fields were formed by averaging the hours 0200–0300–0400 UTC (related to the timing of ascending path), and the hours 1300–1400–1500 UTC (descending path), from each daily simulation, to form a continuous time series of twice-daily fields.

The ARPS model is a regional nonhydrostatic atmospheric model (Xue et al. 1995), and its implementation was essentially the same as that described by Samelson et al. (2002). The model domain configuration included coarse and nested horizontal grids with 36- and 12-km grid boxes, respectively. The vertical grid had 31 levels from the surface to nearly 14-km height, with the first model layer at 10 m. The higher-resolution inner nest was centered on Newport, Oregon, and the results from this grid were analyzed in the study. NCEP Eta Model fields were used for initial and outer nest lateral boundary conditions. The ARPS utilizes a 1.5-order Deardorff TKE-based subgrid-scale turbulent closure (Deardorff 1980: Moeng 1984). The PBL parameterization, including surface fluxes calculated from stability-dependent bulk formulas, follows Sun and Chang (1986). Wind stress components were included in hourly archived model output. As for COAMPS, 3-h averages of surface stress wind fields were computed to form the time series to be analyzed.

The QuikSCAT data grid and the three model grids all differed. Thus, it was necessary to perform interpolations in order to conduct some of the comparative analyses discussed later. The details of the interpolations
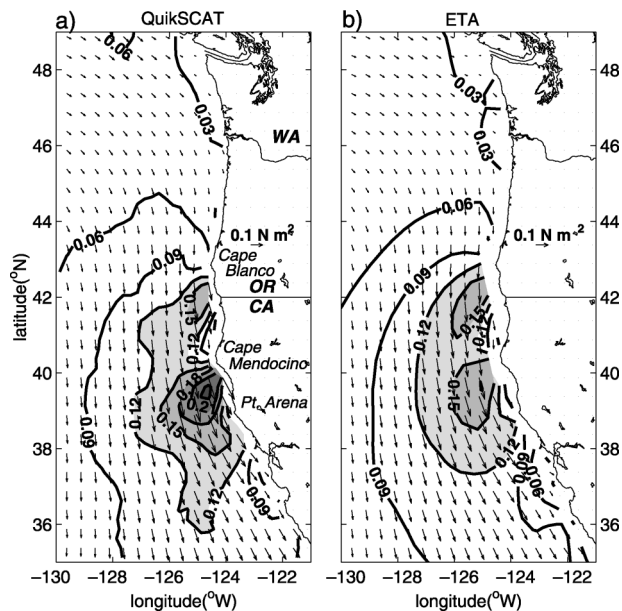

FIG. 1. Mean wind stress vector direction and magnitude (N m^{-2}, see insert) for (a) QuikSCAT, (b) Eta modeled stress, Jun–Sep 2000 and 2001. Eta contours are for the model field on a 40-km grid, while Eta wind stress vectors are linearly interpolated onto the QuikSCAT 0.25° grid, for easy visual comparison. Only every second stress vector, on the meridional and zonal grids, is shown.

are given in the corresponding sections. Note also that the following abbreviations will be used for the two higher-resolution models: COAMPS will be referred to as HR1, and ARPS as HR2. This is done to emphasize that the present comparisons are limited to the specific implementations of these models used in our study. Note that HR2 was initialized with the initial fields from the same Eta simulations that were used for the Eta statistical comparisons, while HR1 was initialized with fields from a different global model.

3. Large domain: QuikSCAT and the Eta Model

a. Mean wind and wind stress fields

In this section, surface wind and wind stress are considered in a domain that extends meridionally from 35° to 49°N, and zonally from the U.S. west coast offshore to 130°W. In this region, the magnitude of the mean scatterometer wind stress for June–September 2000 and June–September 2001 varies by a factor of 8, from less than 0.03 N m^{-2} in the northeast to more than 0.24 N m^{-2} near 39°N, 125°W, southwest of Cape Mendocino (Fig. 1a). The minimum number of observations per grid point for computing the mean values was set to 100. The large-scale maximum covers the region between 35° and 43°N, and between 124° and 128°W. To the north, the mean stress decreases rapidly between 42° and 45°N, and remains roughly constant from 45° to 49°N. Superimposed on the larger-scale maximum are local maxima, which likely are associated with the

coastline geometry and coastal topography. Wind stress exceeds 0.17 and 0.24 N m^{-2} to the southwest of Cape Blanco and Cape Mendocino, respectively.

The large-scale stress maximum is consistent with the previous analyses of the large-scale wind field along the U.S. west coast (e.g., Halliwell and Allen 1987: Bakun and Nelson 1991). It arises from the intensification of the pressure gradient between the east Pacific high, which in summer is typically centered around 35°N, 145°W, and the continental thermal low, which is typically centered over the southwest United States and extends in a narrow trough toward 40°N, 120°W (e.g., Huyer 1983 her Fig. 1). An alternative explanation exists that relates this large-scale maximum to marine atmospheric boundary layer (MABL) adjustment to the large-scale bend in the California coast (Edwards et al. 2002).

The local maxima downstream of Cape Blanco and Cape Mendocino are related to orographic effects in the inversion-topped MABL, analogous to expansion fans that occur in hydraulically supercritical channel flow in a channel with downstream variation in depth (Winant et al. 1988; Burk and Thompson 1996; Samelson 1992; Samelson and Lentz 1994; Rogerson 1999; Burk et al. 1999; Dorman et al. 2000; Koračin and Dorman 2001; Edwards et al. 2001, 2002). The expansion fan is associated with divergence in the fast horizontal flow on the leeward side of coastal promontories, shallowing of the MABL, and flow acceleration to high values of Froude number.

The general structure of predicted mean wind stress from the Eta Model (Fig. 1b) is very similar to the QuikSCAT wind stress field. It shows excellent agreement with the scatterometer in the directions of the mean vectors, and generally good agreement in their magnitude over most of the domain, but differs in its representation of the local maxima. In the Cape Blanco region, the Eta Model peak magnitudes of the wind stress are close to QuikSCAT values; the differences in the locations of this maximum are discussed further later. In the local maximum on the lee side of Cape Mendocino, the Eta Model underestimates the peak mean observed stress by nearly 30%. Overall, the Eta field is also smoother than the QuikSCAT field.

The orographic intensifications near Cape Blanco and Cape Mendocino are displaced roughly 50 km northward and offshore in the Eta Model, relative to QuikSCAT (Figs. 1. and 2), a distance comparable to one model output grid cell. In the zonal cross section of meridional stress along 42.125°N, the maximum Eta stress occurs near 125.5°W, and the maximum QuikSCAT stress is inshore of 125°W (Fig. 2a). The most evident discrepancy is in the underestimation of the Cape Mendocino stress maximum in the Eta Model, relative to QuikSCAT, which is especially apparent in the meridional cross section of meridional stress along 125.125°W (Fig. 2b). This underestimation and offshore displacement of the peak stress in local maxima are
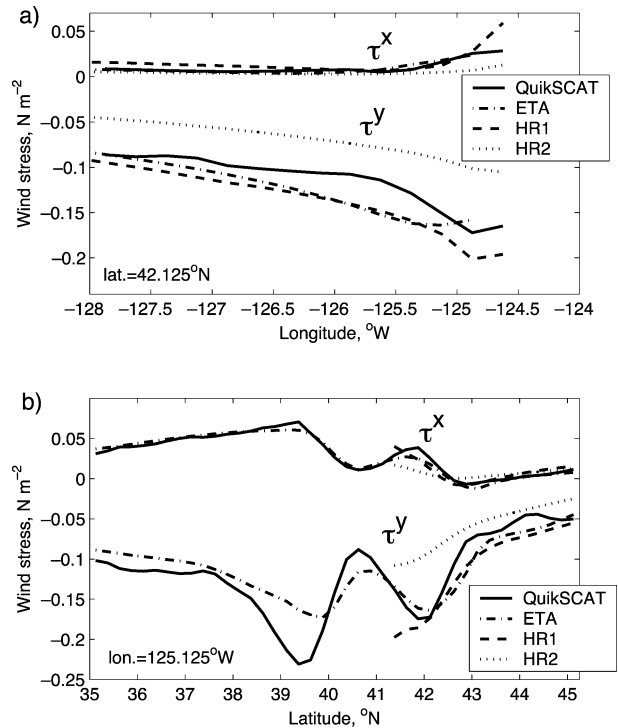

FIG. 2. Mean meridional and zonal stress along (a) 42.125°N and (b) 125.125°W, for the QuikSCAT and three atmospheric models, using the twice-daily time series during the entire study period: 20 Jun–30 Sep 2000, 1 Jun–30 Sep 2001.

likely due to the limitations in model resolution (see discussion in section 4a).

The robust nature of the high-speed maximum off Cape Blanco and Cape Mendocino suggests the frequent occurence there of supercritical or transcritical flow during the summer. These features extend 100–150 km offshore. In contrast, it is interesting to note that the orographic intensification around Point Arena originally identified by Winant et al. (1988) had scales of only 10–50 km, and is not resolved by either the scatterometer or the model fields considered here. The scatterometer analysis displays a certain stretching towards the southeast of the wind maximum associated with Cape Mendocino, which could be an effect from Point Arena. However, it extends much farther offshore from Point Arena than the features observed by Winant et al. (1988; see also Enriquez and Friehe 1995), and is barely detectable in the Eta Model.

b. Correlation analysis

Complex correlations (Kundu 1976) and vector correlations (Crosby et al. 1993) of the scatterometer and Eta Model wind stress fluctuations were computed at each point in the domain (Fig. 3). For this comparison, the model fields were interpolated onto the QuikSCAT 0.25° grid. Correlations near the coast were mostly computed from incomplete time series, because of missing
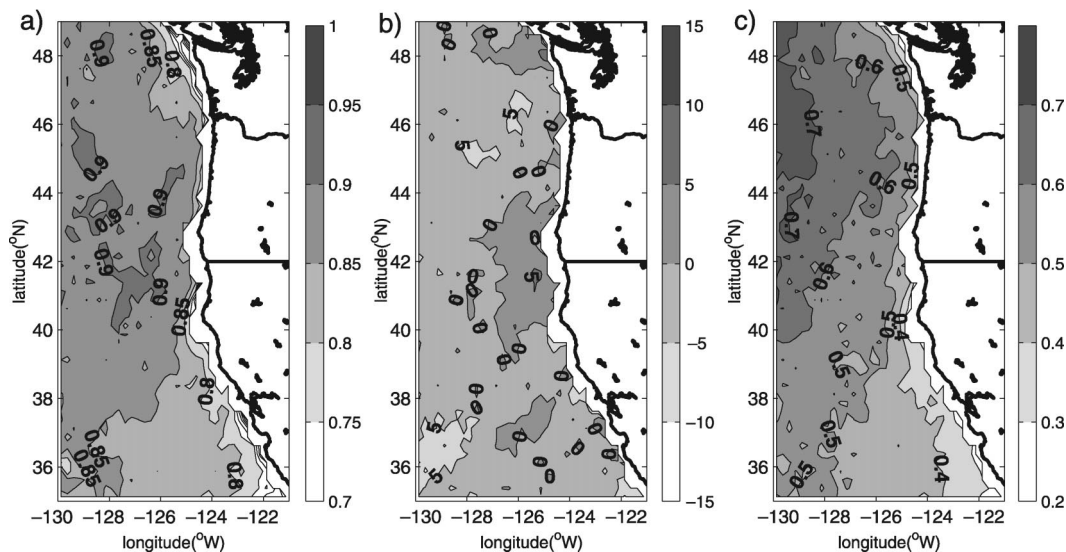
FIG. 3. Correlations between Eta and QuikSCAT stress: complex correlation (a) amplitude, (b) phase, and (c) vector correlation.

scatterometer data, as noted in section 2a. The number of model–observation pairs used to compute the correlations exceeded 400 far offshore, decreasing to less than 400 towards the land, dropping to 100–200 at the nearest inshore points; the minimum number of pairs was 83.

The complex correlation amplitudes exceed 0.85 to the north of 40°N, except near the coast and in a region extending west to 127°W off Washington (Fig. 3a). Between 35° and 40°N, the complex correlations are roughly 0.8–0.85, and lower inshore. Complex correlation phases, or, in other words, mean directional errors, are generally near 0, exceeding ±5° in only a few locations (Fig. 3b).

Vector correlations were computed according to the definition by Crosby et al. (1993), and normalized by 2 to yield values in the range 0 to 1. The correlations decrease systematically toward the coast and southward, varying from greater than 0.7 in the northwest to less than 0.4 in the southeast (Fig. 3c). This decrease is evidently due to the greater directional steadiness of the winds in the south, which align more consistently along-shore. Since the signal-to-noise ratio in the variability of the cross-shore component is small, this lowers the vector correlation.

The lower correlations adjacent to the coast may also arise from limitations of the model prediction where surface conditions change abruptly from land to water grid points, or from the interpolation from the computational model grid to the output grid, which may mix land and sea effects across the land–sea boundary.

c. Stability effects

The scatterometer measures the radar backscatter from sea surface roughness elements and is more di-

rectly related to the surface stress than to the wind above the sea surface. For a given value of stress, the wind speed above the sea surface depends on atmospheric stability, while the measured radar backscatter will not. Since stability information is generally not available, the scatterometer measurements are provided as an equivalent neutral stability wind speed.

The effect of atmospheric stability on the wind profile in the surface layer is often parameterized by similarity theory in the form

$$U_z - U_0 = (u_*/\kappa)[\ln(z/z_0) + \Psi(z/L)], \quad (3.1)$$

where U_z is the wind speed at height z, U_0 is the wind speed at the surface (either 0, or the speed of the surface current), u_* is the friction velocity, κ is the von Kármán constant, z_0 is the aerodynamic roughness length, and $\Psi(z/L)$ is the stability term, where L is the Monin–Obukhov length (Fleagle and Businger 1980). Under neutral conditions, the stability term is 0, and the expression reduces to a logarithmic wind profile. This profile is used to compute the equivalent neutral stability winds. For stable conditions, usually found over the region of interest in this study, the equivalent neutral winds are smaller than winds by an anemometer. For unstable conditions, equivalent neutral winds are greater than anemometer winds.

The equivalent neutral stability 10-m winds were computed from the wind stress or model friction velocity fields using Eq. (3.1) with a roughness length corresponding to the Large and Pond (1982) neutral drag coefficient (Fig. 4). Eta results are similar to those of QuikSCAT, with the equivalent neutral stability winds slightly overestimated by Eta southwest of Cape Blanco and underestimated by 0.5 m s^{-1} in the wind maximum southwest of Cape Mendocino. Eta 10-m "anemometer" winds (not shown) are smaller than Eta equivalent
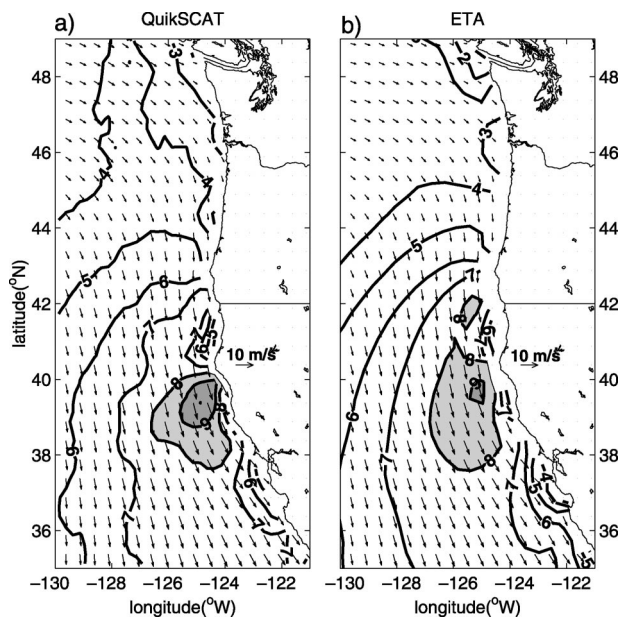
FIG. 4. Mean surface (10-m) winds (m s^{-1}, see insert): (a) QuikSCAT equivalent neutral stability, (b) Eta equivalent neutral stability winds derived from wind stress. Eta winds are interpolated to QuikSCAT 0.25° grid; only every second wind vector, on the meridional and zonal grids, is shown. Areas with the mean wind magnitudes above 8 m s^{-1} are shaded.

FIG. 5. (a) Mean sea surface temperatures (SST) (K), and (b) mean differences (K) between the 10-m air temperature and the SST, from the Eta Model.

neutral stability winds (Fig. 4b) by 0.5–1 m s^{-1} nearly everywhere southward of 44°N. These results are consistent with the near-surface stability estimates, inferred from the differences between the model 10-m air temperature and the sea surface temperature (SST; Fig. 5). Air temperature–SST differences are negative over most of the domain (unstable conditions) but approach 0 and even become positive (stable) in the coastal zone between Cape Blanco and Cape Mendocino where the coldest water is located.

Note that from the oceanographic point of view, it is the wind stress that is of interest. When using modeled 10-m winds to estimate the surface wind stress, the appropriate stability adjustment is needed. Calculation of wind stress from anomemeter winds without adjusting for stability effects will lead to a wind stress that is biased systematically low. For atmospheric studies, however, a stability correction is needed to estimate the lower-tropospheric winds from the available scatterometer observations.

4. Oregon coastal zone: QuikSCAT and models

a. Mean fields

An area of particular emphasis for this study is the Oregon coastal zone. Wind-driven coastal ocean upwelling circulations in this region have been an object of scientific interest and research since the Coastal Upwelling Experiment (CUE) in 1972 and 1973 (Smith 1974; Halpern 1976). Recently, intensive oceanographic
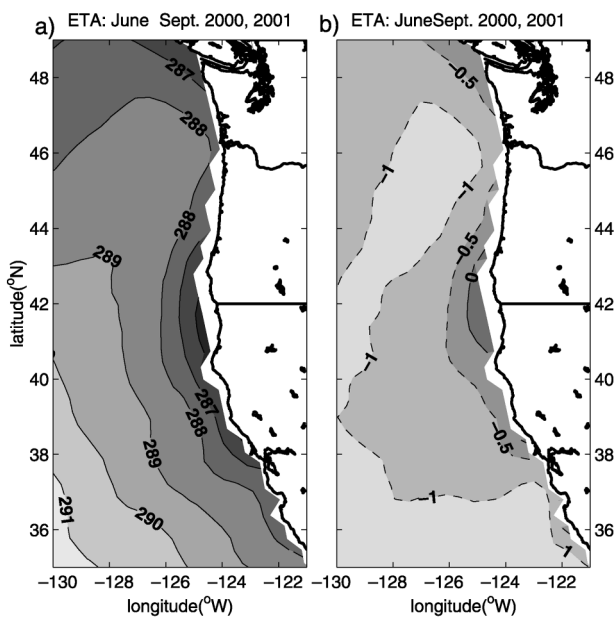
observational programs were carried out during summers 1999 and 2001. In support of these programs, the HR1 and HR2 high-resolution mesoscale atmospheric models were implemented for this region as described in section 2b. These models provide two additional estimates of the wind stress field in the Oregon coastal zone during summers 2000 and 2001.

The dominant feature in the mean and fluctuating summertime wind stress fields in the Oregon coastal zone is the region of intensified stress southwest of Cape Blanco (Fig. 6; see also Fig. 2). This feature appears in the QuikSCAT observations and in all three model fields, but varies in its amplitude, spatial scales, and location. The most extreme stress values from these four estimates are obtained from the two high-resolution regional models. In the HR1 model fields, peak mean stress near Cape Blanco reaches 0.24 N m^{-2}, yielding strong wind stress gradients in the narrow coastal zone. This is larger than the 0.17 N m^{-2} maximum wind stress in the QuikSCAT data. In the HR2 model, peak mean stress only slightly exceeds 0.12 N m^{-2}. The weaker mean wind stress from the HR2 model, relative to the other three estimates, arises from a weaker meridional wind component (Fig. 2).

Compared with the scatterometer measurements, the location of the axis of maximum stress extending southwestward from Cape Blanco is best represented, relative to the scatterometer measurements, in the high-resolution models. The HR1 model places the wind stress maximum closer inshore and partially confined within 50 km off the coast (Fig. 6c, 0.21 N m^{-2}). The Eta Model places this axis roughly 50 km to the northwest of its observed location. Note that the mean wind stress vectors are
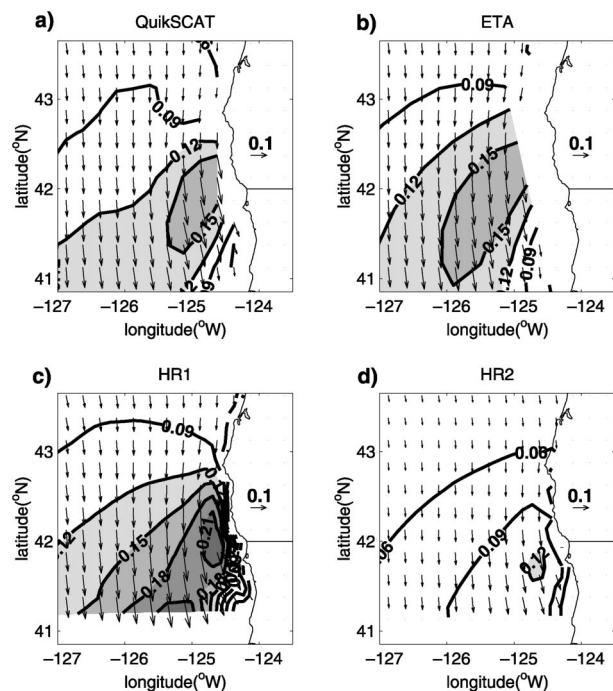
FIG. 6. Mean wind stress vector components and magnitude (N m^{-2}, see insert) near Cape Blanco for (a) QuikSCAT, (b) Eta, (c) HR1, and (d) HR2, Jun–Sep 2000 and 2001. Contours are plotted for the fields on corresponding model domain grids (inner nest grids for HR1 and HR2). The wind stress vectors are linearly interpolated onto the QuikSCAT 0.25° grid. Contour interval is 0.03 N m^{-2}.

aligned ≈45° counterclockwise from the axis of maximum stress, except in the HR1 isolated local maximum in the coastal zone, and thus do not have a jetlike structure. The offshore displacement of the axis of maximum wind by the Eta Model is not large relative to the resolution of the QuikSCAT measurements or the Eta grid, but it is large compared to the dynamical scales of the coastal ocean upwelling circulation, which are often shorter than 10 km near fronts and jets and immediately adjacent to the coastal boundary. The associated wind stress curl fields, which have important implications for ocean circulation, are discussed in section 7.

b. Correlation analysis

Complex correlations between the HR2 model stress and the QuikSCAT observations (Figs. 7e,f) are mostly similar to those between Eta and QuikSCAT (Figs. 7a,b). In some places HR2 shows relatively lower correlations than Eta, see, for example, the complex correlation amplitudes south of 44°N. The mean directional offset (phase) relative to QuikSCAT at the location of the wind maximum downwind of Cape Blanco is 5°–10° for HR2 (Fig. 7f), and 0°–5° for Eta.

The HR1–QuikSCAT complex correlation amplitudes are noticeably lower, especially adjacent to the central and northern Oregon coast in the northeast part of the
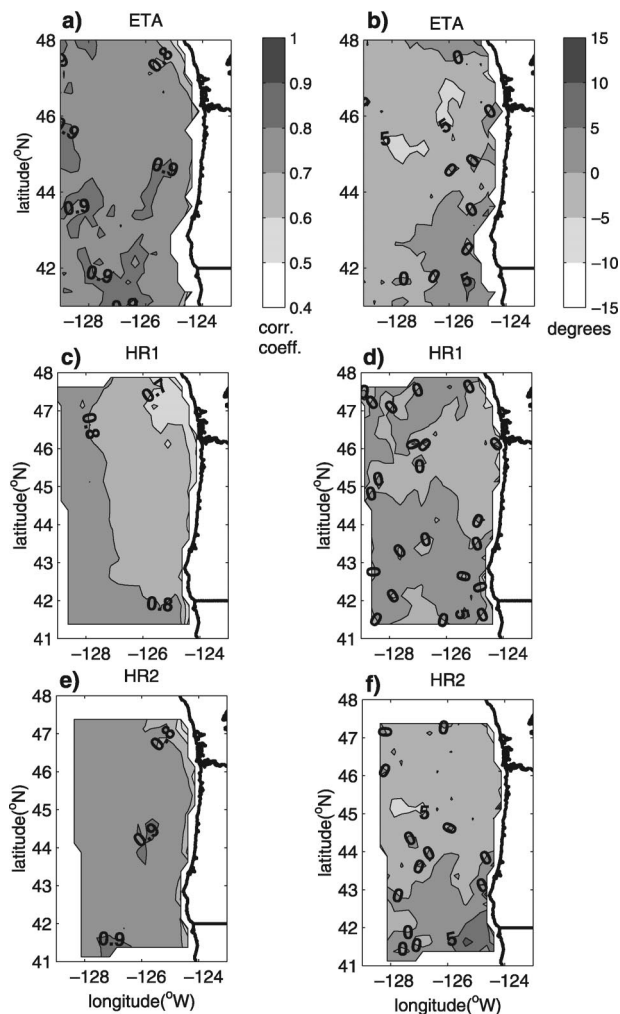

FIG. 7. Complex correlation (left column) amplitude and (right column) phase of the wind stress between the models and QuikSCAT. Jun–Sep 2000 and 2001, on a smaller domain. (a),(b) Eta; (c),(d) HR1; (e),(f) HR2 model. Model fields were linearly interpolated onto the QuikSCAT 0.25° grid to compute the correlations. The number of model–observation pairs was over 400 far offshore, less than 400 toward land, and 100–200 at the last point inshore. The minimum number of pairs was 83 for Eta, 46 for HR1, and 52 for HR2.

domain of the regional model (Figs. 7c,d). The correlation phase difference between HR1 and QuikSCAT, however, is smaller than the others, oscillating near 0, and exceeding 5° only in the single location off northern California at ≈41.5°N.

The complex correlations between model and QuikSCAT are usually lower for wind stress than for the corresponding equivalent neutral stability winds (Fig. 8a). The decrease in correlations with scatterometer stress from south to north is more pronounced for HR1, less evident for the HR2 model, and nearly nonexistent for the Eta. In the equivalent neutral stability wind correlations, the northward decrease is well defined for HR1–QuikSCAT, but much less apparent for the other two models (Fig. 8a). Correlations of 10-m
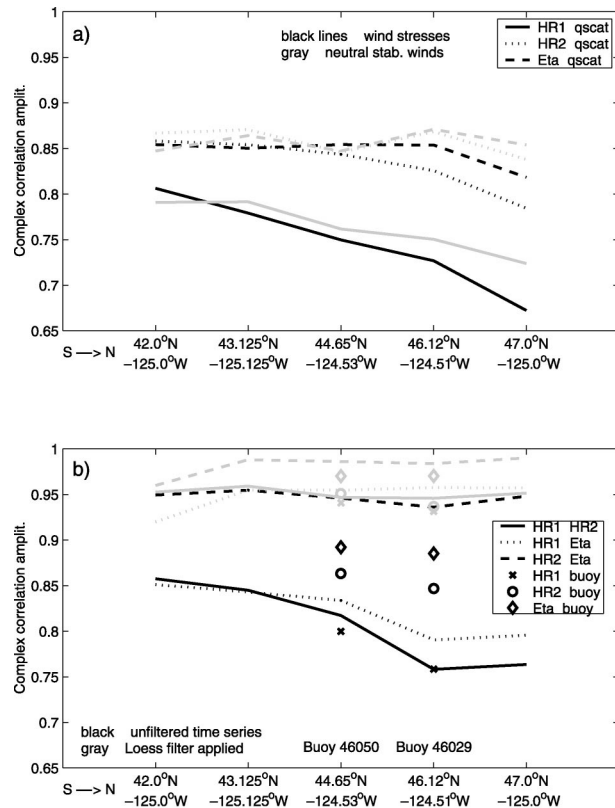
FIG. 8. (a) Complex correlation amplitudes between QuikSCAT and model time series for Jun–Sep 2000, 2001 vs alongshore location. Wind stresses (black lines), neutral stability winds (gray lines). (b) Complex correlation amplitudes of 10-m anemometer winds 1 Jun–30 Sep 2001, between the models and between model and buoy hourly (3 h for Eta) time series vs alongshore location. Unfiltered winds (black lines), loess low-pass filter applied with 10-day half-span (gray lines).

model winds with winds from the two buoys along the central and northern Oregon coast are consistent with the scatterometer–buoy correlations, as are model–model correlations (Fig. 8b). The same time series, smoothed with a low-pass loess filter with 10-day half-span (the locally weighted quadratic regression, developed by Cleveland, 1979; see also Schlax and Chelton 1992), show increased correlations for all the models, and nearly no alongshore dependence (Fig. 8b). The low HR1 correlations therefore arise from fluctuations at frequencies higher than 0.1 cpd.

Some of the similarity between the Eta–QuikSCAT and HR2-QuikSCAT correlations may arise from the use of the Eta fields to initialize the HR2 model, and to provide lateral boundary conditions for the outer (36-km) HR2 grid. On the other hand, these two models produce different results for the diurnal cycle in the near-coastal region (section 5).

c. Spectral analysis

Spectral decomposition of the surface wind at the location of National Data Buoy Center (NDBC) buoy

46050 (44.65°N, 124.53°W) was performed for the hourly time series from the buoy and the three models, for the period 1 June–30 September 2001 (Figs. 9a,b). Buoy 5-m winds were logarithmically adjusted to a standard 10-m height. Out of total 2928 time records, there were 10 gaps, mostly of 1–2 h each and a single 4-h gap, that were filled by linear interpolation to obtain continuous time series. For the models, the successive model forecasts were combined into one long time series for the studied period. Eta used the forecast hours 3 to 24 with 3-h interval; HR1 and HR2 models used hourly forecasts from hour 2 to 25. Time series were normalized prior to the spectral decomposition; block averaging was used with a minimum of 50% segment overlap and a Hanning window applied to data segments. Same number of degrees of freedom was chosen for all of the time series, resulting in a single bar of confidence interval per panel.

Most of the power is contained in the low-frequency part of the meridional wind component (Fig. 9). These low frequencies represent the synoptic-scale contribution. While the spectral peaks at 1 and 2 cpd represent diurnal and semidiurnal fluctuations respectively. For the zonal wind (*U*-wind), the variance contribution from low frequencies is comparable to that from diurnal fluctuations of both the zonal and meridional winds (*V*-wind). The peak at 2 cpd is identifiable but weaker.

Squared coherences computed between the model and buoy winds (Figs. 9c,d) are high at low frequencies for the *V*-wind; for the *U*-wind they are notably lower, and are below the 95% significance level in some bands for both HR1 and HR2. Well-defined coherence peaks appear at 1 cpd for both wind components, as well as at 2 cpd in the *U*-wind. The Eta winds are generally less energetic than the others (Figs. 9a,b), but their coherences with the buoy winds consistently exceed those of the higher-resolution models (Figs. 9c,d). The average phase lag (not shown) relative to the buoy winds at 1 cpd is largest for Eta, exceeding 2 h, and is roughly 1 h for HR1 and HR2 (confidence intervals are about ± 1 h for all). The decrease in coherence between 0.2 and 1 cpd in the *V*-wind (Fig. 9d) is especially rapid for HR1.

The merdional variations in the wind spectra can be characterized by comparing the average power spectral density at frequencies 0.09, 0.55, and 1 cpd at five alongshore locations (Fig. 10). The first two bands are both high in variance content, but differ greatly in coherence with the buoys, while the 1 cpd band contains the energetic diurnal cycle along most of the coast. The most prominent feature is the northward decrease in the power of the meridional wind component at low frequencies (0.09 cpd), consistent with the large-scale circulation pattern associated with the east Pacific high and the continental thermal low. The *V*-wind power density at 0.55 cpd is moderately high and about the same everywhere, and is close to that of the synoptic-scale *U*-wind power density. The *U*-wind power density at 0.55 cpd
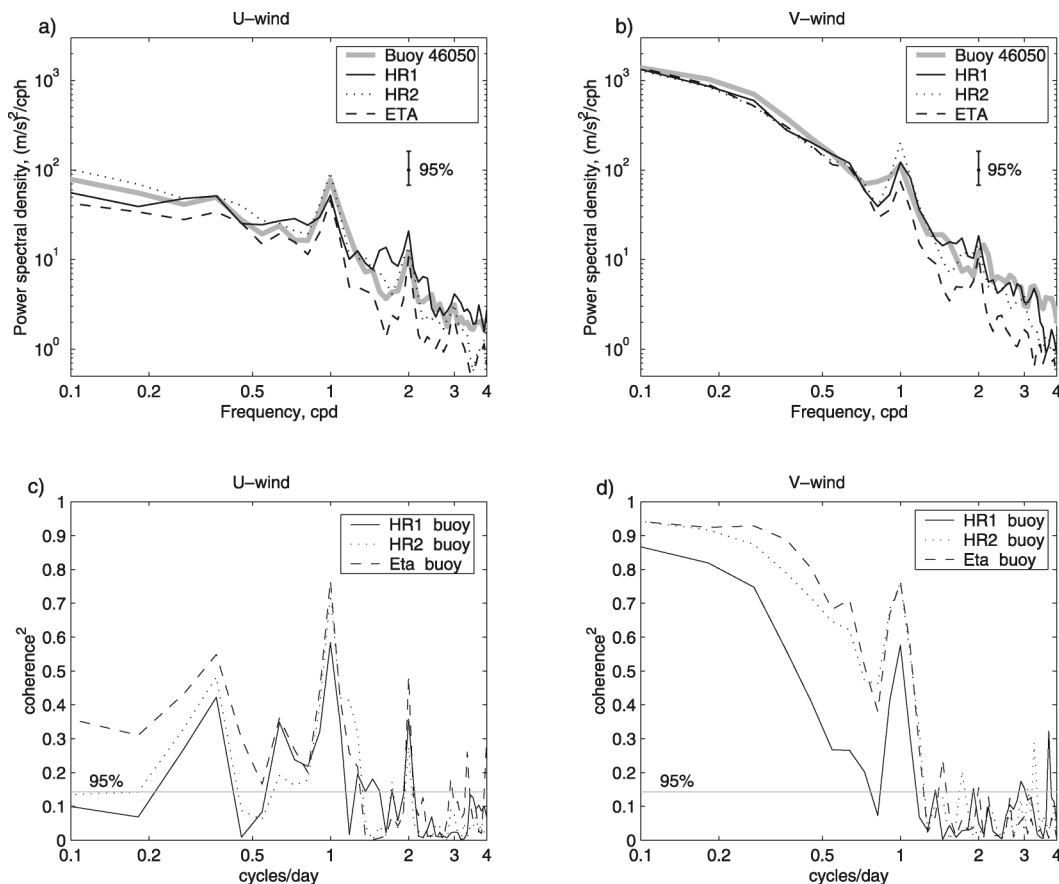
FIG. 9. (a),(b) Power spectral density of (left) zonal and (right) meridional components of model and NDBC 46050 buoy 10-m winds, at the buoy location with lat = 44.65°N, lon = 124.53°W, for 1 Jun–30 Sep 2001: (c),(d) squared coherences between the models and the buoy observations of the corresponding wind components.

steadily increases northward and becomes the same order of magnitude as that from diurnal fluctuations north of about 45°N.

Squared coherences between the models, and between the models and the NDBC buoys 46050 and 46029 were computed for the same bands and locations (Fig. 11). Except for the synoptic-scale V-wind, the coherences between HR1 and the other models and the buoys are consistently lower, especially at 0.55 cpd. The variance contributions to the meridional wind at low frequencies are well represented and highly coherent between all of the models. This low-frequency variance decreases northward, resulting in a corresponding increase in the contributions from the higher frequencies that are less coherent between the models and buoys. The HR1 model was shown to be notably less coherent with the buoy data than the other models at higher frequencies, consistent with the northward decrease in HR1–QuikSCAT complex correlations in the coastal area. These results motivated the earlier choice of the 10-day half span for the loess filter, which retains the variance at frequencies lower than 0.1 cpd.

We considered the possibility that the reduced correlations for HR1 may have been due to the errors in the daily initialization and boundary data obtained from the global NOGAPS model, relative to those obtained from the Eta Model, which were also used as initialization and boundary data for HR2. However, correlations computed directly from the NOGAPS fields during summer 2001 were comparable to those from the Eta Model, precluding this possibility. This result is consistent with the conclusions drawn from the coherence analysis.

5. Diurnal cycle

Estimates of the diurnal evolution of wind stress were obtained from NDBC buoy 46050 and the three models (Fig. 12; see also Samelson et al. 2002, their Fig. 7b), and from the approximate twice-daily QuikSCAT passes over the study region, which occur near the extreme phases of the diurnal cycle (Fig. 12). Significant differences between the models are apparent in the estimation of the daily mean meridional wind stress component, but the diurnal variations are relatively consistent between the models. The QuikSCAT and Eta Model
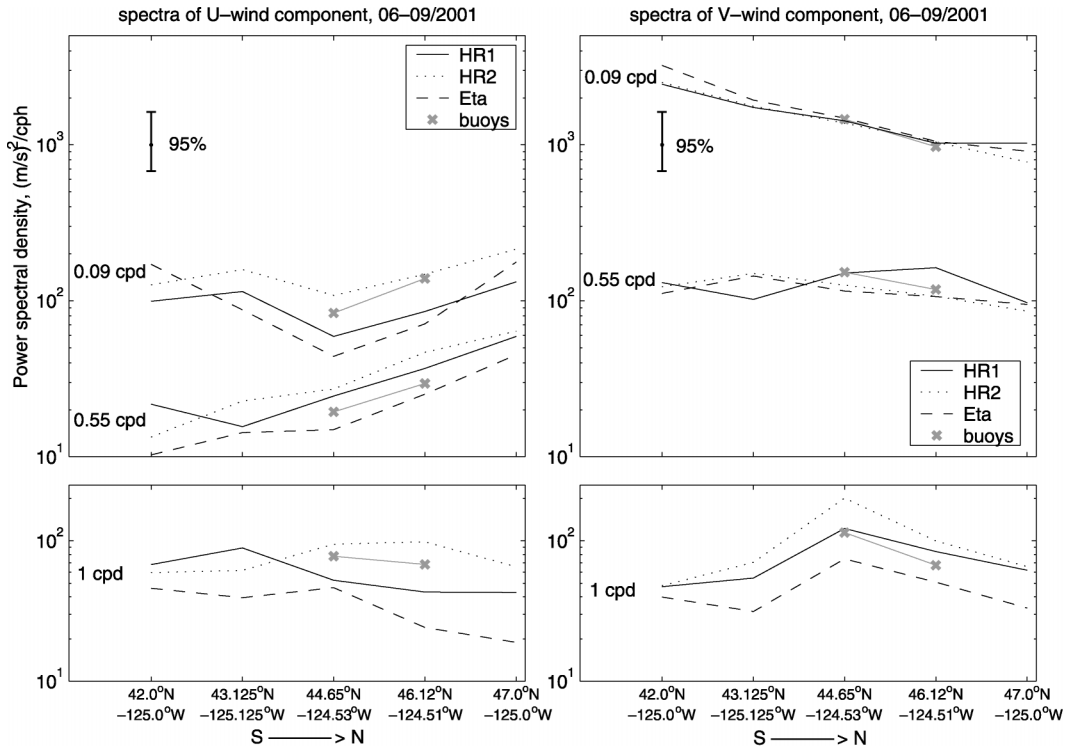
FIG. 10. Power spectral density of (left column) zonal and (right column) meridional model and buoy 10-m wind components for the three spectral bands: (top) 0.09 and 0.55 cpd, (bottom) 1 cpd at several alongshore locations, south to north.

diurnal stresses are nearly 0.015 N m^{-2} higher than the buoy stress; these differences are likely due in part to differences in spatial resolution in the presence of a cross-shore gradient in stress near the coast. Note that the Eta Model, with horizontal grid scale close to the

nominal QuikSCAT resolution, yielded the estimate of the wind stress diurnal evolution that was most consistent among the three models with the QuikSCAT measurements at this location.
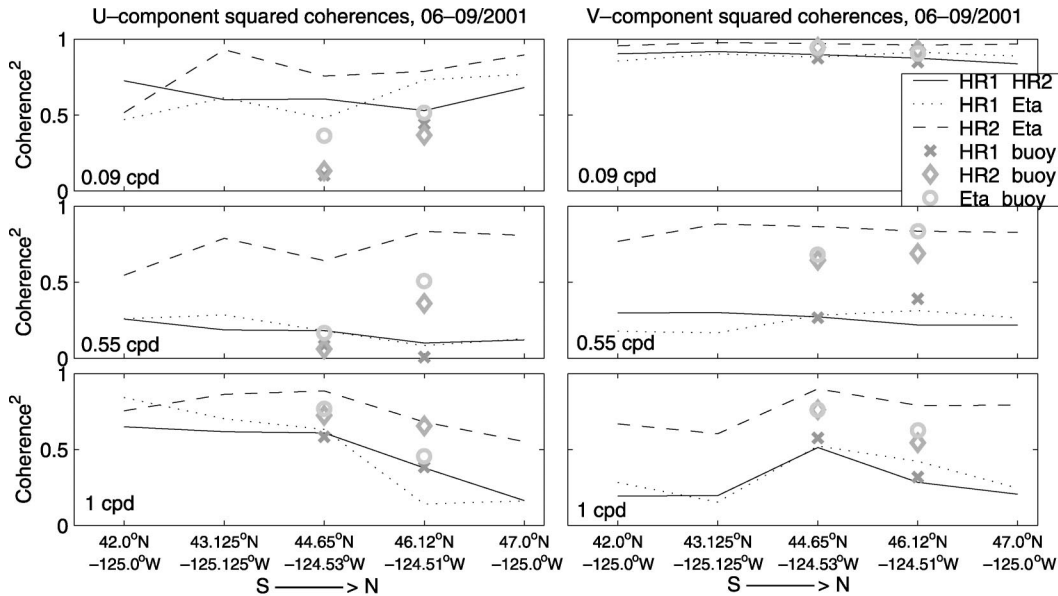
Diurnal fluctuations were computed for the 2D

FIG. 11. Squared spectral coherences corresponding to the same spectral bands and locations as in Fig. 10.
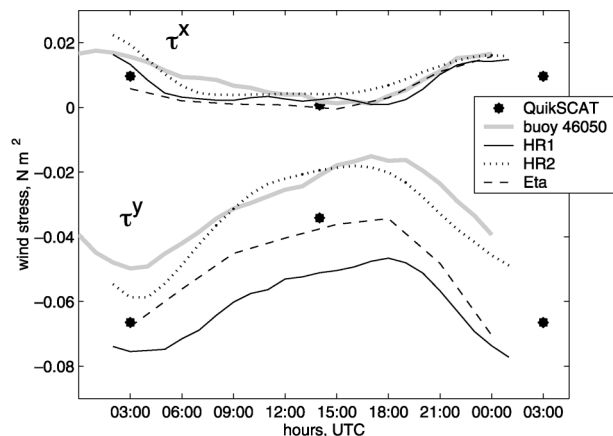
FIG. 12. Mean diurnal evolution of QuikSCAT and models wind stress components at the location of NDBC buoy 46050. The buoy wind stress was computed using the neutral stability drag coefficient from Large and Pond (1982).

QuikSCAT grid, by differencing evening and preceding morning observations, by differencing evening and successive morning observations, and computing the mean value of all the resulted differences at each grid point. A minimal threshold of 150 difference pairs at each location was chosen to obtain reliable estimates of the mean values. Gille et al. (2003) have used similar techniques to estimate diurnal circulation from global QuikSCAT data.

The result (Fig. 13a) reveals a surprisingly strong diurnal cycle with southward–southeastward wind stress greater in the evening than in the morning in a coastal zone that extends offshore about 150 km north of 42°N, but only about 50–100 km south of 39°N. The region of detectable diurnal variability extends offshore about 300 km to 128°W near 42°N. Diurnal variability is restricted to a very narrow region just south of Cape Mendocino. Between 40° and 42°N, the sense of the diurnal circulation reverses, with stronger southward winds in the morning than in the evening. The evening diurnal circulation converges near 41.5°N in a region where the diurnal flow is strongly onshore in the evening. This circulation is likely driven by enhanced heating over the high orography of northwestern California, as speculated by Bielli et al. (2002). Mean evening–morning differences reach or exceed 0.05 N m^{-2} in the narrow coastal zone just offshore and south of the Oregon–California border, and also halfway between Cape Mendocino and Point Arena. Oceanographic effects of diurnal stress variations can be significant (e.g., Lerczak et al. 2001), and need further investigation.

Corresponding estimates of the diurnal cycle from successive evening–morning differences of the Eta Model wind stresses at the approximate times of QuikSCAT passes show some general similarities, including the convergence of the diurnal circulation at the correct latitude, near 41.5°N (Fig. 13b). The diurnal intensifications of the northwesterly flow in the coastal

zone downwind of Cape Blanco and Cape Mendocino, however, are notably weaker than in QuikSCAT observations, and the model circulation is also more closely confined to the coast, extending offshore no farther than 150 km near 42°N. The weaker diurnal cycle for Eta could be due in part to underestimation of the evening winds (at 0300 UTC, only 3 h after the model initialization), arising from an incomplete spinup of the circulation. In support of this speculation, the amplitudes of the cycle increase when the next-day evening estimates (0300 UTC, 27-h forecasts) are used to compute the diurnal cycle (not shown).

Similar computations for HR1 and HR2 model results show that the high-resolution mesoscale models do not provide more accurate representations of the diurnal cycle along the Oregon coast (Fig. 14). The offshore extent of the HR1 difference vectors is too limited, and the reversal of HR1 cycle occurs off Cape Blanco, at 43°N, about 150 km farther north than observed. These differences contribute to the low HR1–QuikSCAT correlations discussed earlier.

The general sense of the diurnal cycle in the HR2 model agrees with the observations; it gives fairly good estimates offshore between 125° and 126°W, but appears to be too strong closer inshore. Over the HR2 domain, no alongshore reversal of the cycle occurs, but the location of the reversed in the QuikSCAT data coincides with the southern boundary of the HR2 model domain.

6. EOFs

Vector empirical orthogonal functions (EOFs) were computed from the stress fields from QuikSCAT (Fig. 15) and all three atmospheric models for the area along the Oregon coast. Only QuikSCAT time records with over 95% of spatial coverage in the area of interest were used to compute the EOFs. Missing data in these time records (up to 5% of the area per time record, mostly near the boundaries) were filled by linear interpolation or extrapolation from the existing data points. The total number of QuikSCAT time records used for the EOF calculations was 343, and the number of grid points was 584. For these calculations complete time series with the maximal temporal resolution available for each product were used (twice daily for QuikSCAT, 3-hourly for Eta, hourly for HR1 and HR2), in order to extract the best representation of the corresponding variability.

For the first three QuikSCAT wind stress EOFs, the modal contributions to the total variance were 64%, 12%, and 5%, respectively. Local modal contributions, however, differ considerably from the mean in some areas (see the contours in Fig. 15). The leading EOF represents spatially coherent fluctuations in the alongshore wind stress. The structure of the first EOF is similar to the mean stress field, consistent with the previous results of Samelson et al. (2002). This situation occurs because the field tends to fluctuate between states of weak and strong southward stress, so that both the mean
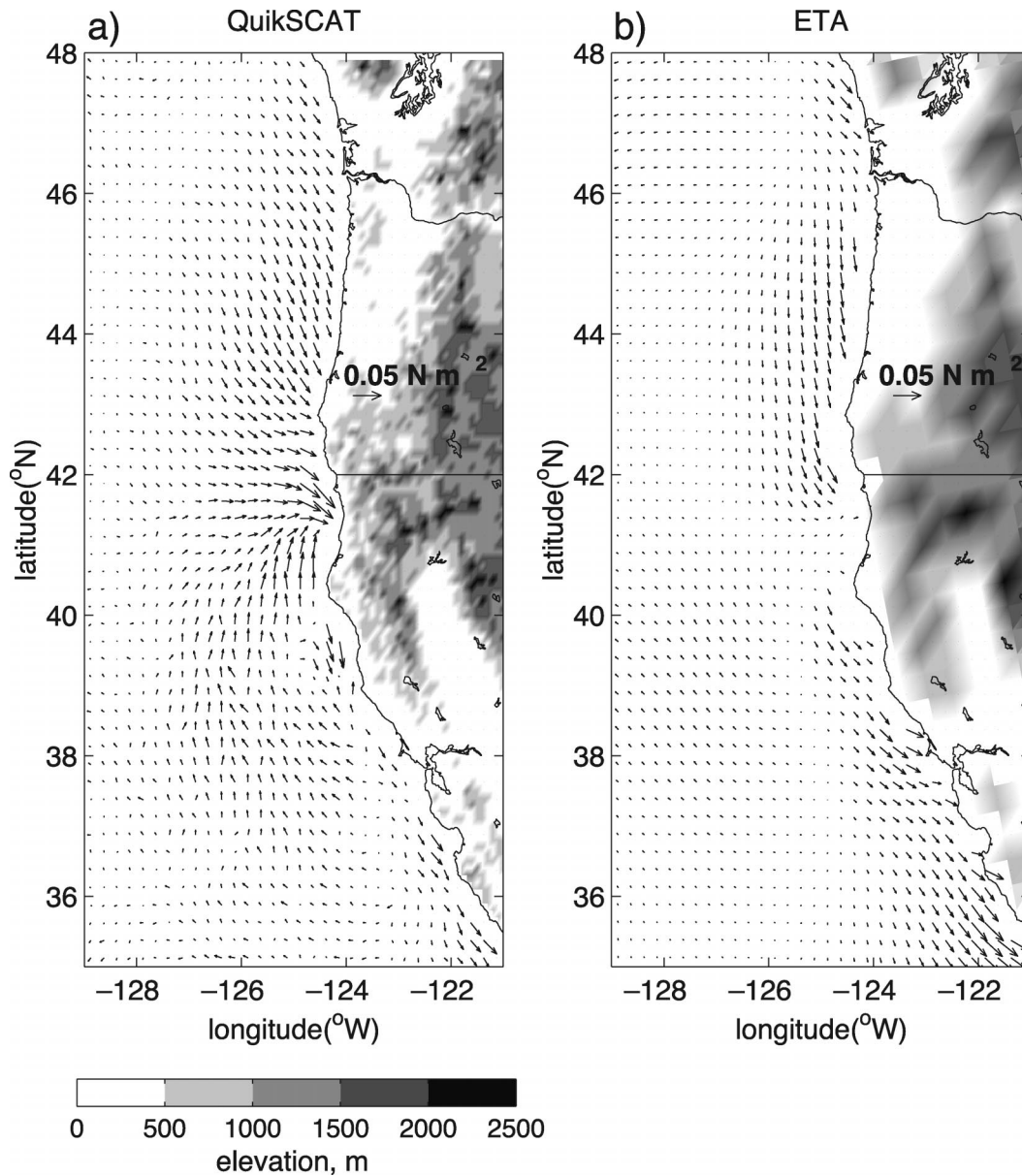
FIG. 13. Mean evening minus morning differences for (a) QuikSCAT and (b) Eta wind stress (N m^{-2}, see insert), Jun–Sep 2000 and 2001. (a) Terrain elev data from USGS 30-arc data linearly interpolated to 0.1° grid; (b) the terrain is from the model grid settings.

and the fluctuating stress are dominated by the structure of the strong southward stress events. These in turn are dominated by the orographic intensification near Cape Blanco. When added to the mean wind stress field, the first EOF corresponds to stronger alongshore upwelling-favorable winds when the amplitude time series is positive, with intensification downwind and offshore of Cape Blanco.

The second EOF mode shows opposing alongshore winds on opposing sides of a 0 line oriented diagonally across the domain from the central Oregon coastline at about 44.5°N to the southwest corner of the domain. At times when the amplitude of this second EOF is positive, the alongshore wind stress is weakened in the northwest part of the domain, and intensified in the southeast part. This second mode has little effect on the stress along the central Oregon coast where the magnitudes of the EOF vectors are all very small and the EOF contribution to the local variance is negligible.

The third EOF predominantly indicates that northwest intensification of the flow in the northwest part of the domain (offshore) corresponds to intensification of the southeast flow in the northeast part of the domain (coastal region).
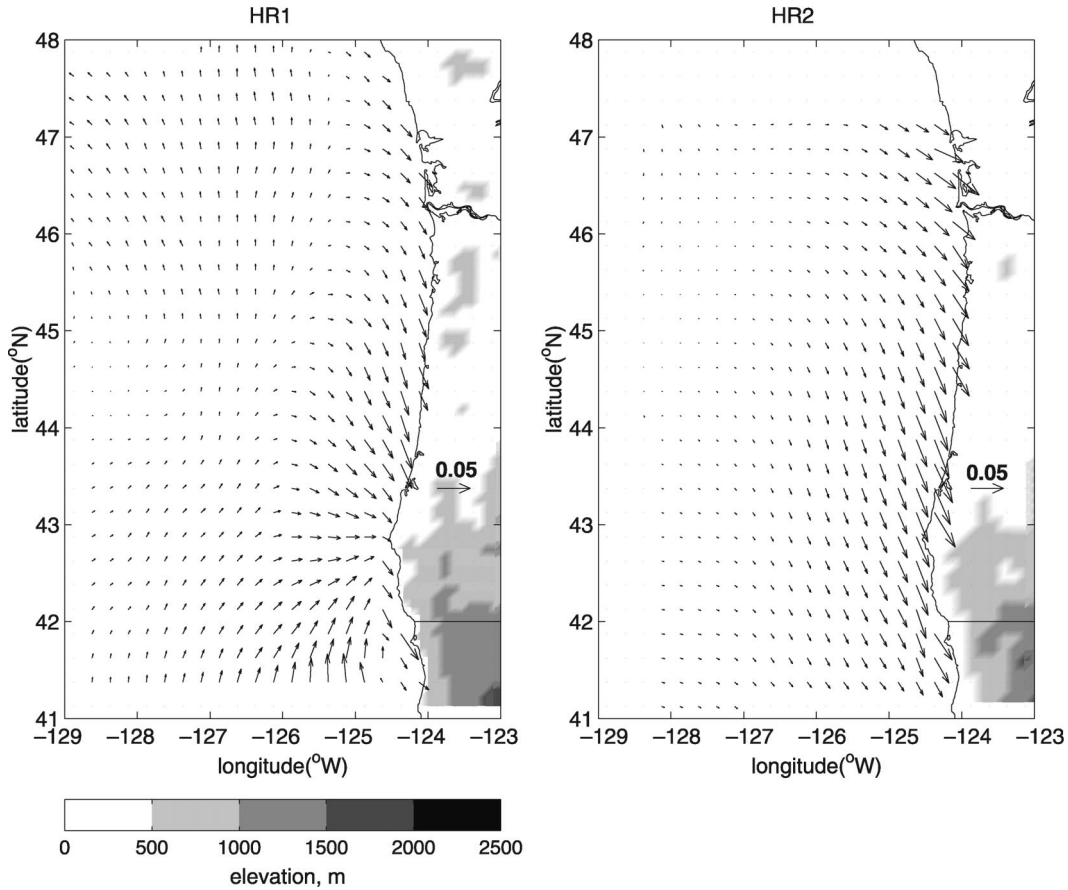
FIG. 14. Mean evening minus morning differences for (left) HR1 and (right) HR2 wind stress (N m^{-2}, see insert), Jun–Sep 2000 and 2001. Terrain elev from the corresponding models.
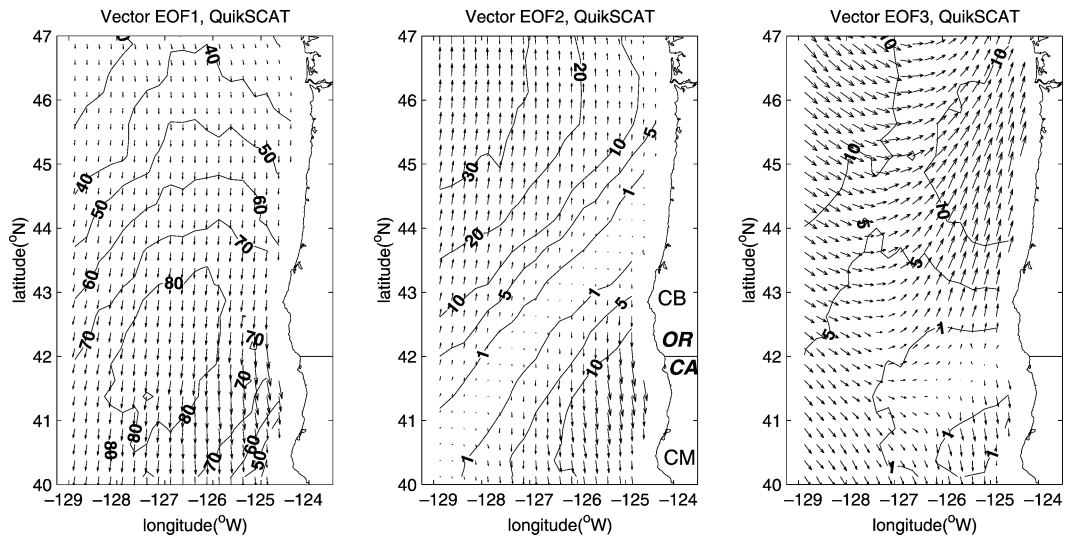

FIG. 15. First three vector EOFs of the QuikSCAT wind stress, overlaid by the contours of the modal contribution into the local variance in percent. CB–Cape Blanco, CM–Cape Mendocino, OR–Oregon, CA–California. See text for details.
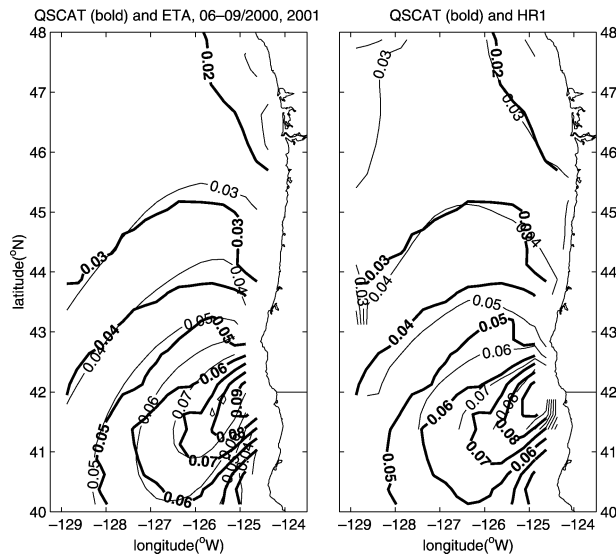
FIG. 16. Magnitude of leading vector EOF of the wind stress: (left) from QuikSCAT (thick contours) and Eta (thin), and (right) from QuikSCAT (thick contours) and HR1 (thin). See text for details.

Similar vector EOFs were computed from the model Eta and HR1 wind stress fields, except that the forecast data for all available times, 3 h and 1 h, respectively, were used. The numbers of grid points used in the Eta and HR1 EOF computations were 570 and 517, and the lengths of the time records were 1733 and 5400, respectively. Comparison of the first EOFs from the models with the QuikSCAT EOFs indicates that the highest-resolution regional model (HR1) most accurately reproduces the location of the axis of maximum variability in stress near Cape Blanco (Fig. 16). However, for the first five modes analyzed, temporal cross correlations between the QuikSCAT and Eta EOF amplitude time series were all higher than the corresponding correlations with the other models (Table 1), consistent with the earlier discussion of mean and fluctuating stress statistics. One potential source of differences between the EOFs is the differing temporal resolution of the QuikSCAT, Eta, and HR1 model fields that were used for these calculations.

Because each QuikSCAT swath samples a fixed area on the surface of the earth, the longitudinal separation between the swaths from neighboring ground tracks decreases with increasing latitude. The temporal coverage at any particular longitude therefore improves with increasing latitude. Consequently, and because the time separation from neighboring swaths presents additional complications, we have not attempted to compute EOFs from the QuikSCAT data over larger regions. Eta Model forecasts were used to compute the EOFs for the area extending farther south to 35°N.

The first wind stress EOF from the Eta Model computed on the large domain (Fig. 17a) is very similar to that of the QuikSCAT wind stress on the smaller domain (Fig. 15a), and explains 56% of the variance. In this

TABLE 1. Temporal correlations (%) of the first five EOF modal amplitudes between the QuikSCAT and the three models in the OR coastal region. Note that while HR1 and HR2 EOF amplitudes had hourly resolution, Eta amplitudes had 3-h resolution, and QuikSCAT amplitudes correspond to the selected passes from twice-daily data. The correlations between the amplitudes were computed using the concurrent times.

Model	EOF 1	EOF 2	EOF 3	EOF 4	EOF 5
Eta	97	92	79	70	60
HR1	91	79	69	53	58
HR2	91	85	66	69	47

first EOF, wind stress in the California coastal region south of Point Arena shows almost no relationship with the wind stress regime farther offshore and to the north. The second EOF represents 24% of the variance (Fig. 17b) and corresponds for positive EOF amplitude to enhanced upwelling-favorable wind stress along the California coast, relative to the Oregon coast. Note that the vector orientation turns eastward to southeastward (alongshore) along a line extending southwest from Cape Blanco, the approximate axis of the wind intensification around Cape Blanco. A similar nodal line along the strongest wind stress axis appears farther south off Cape Mendocino in the third EOF (6.5% of the total variance). Because of different areas involved in EOF decomposition of the QuikSCAT data and of the Eta output over the extended domain, the corresponding higher EOF modes may reflect different spatial relationships, according to the successive eigenvalues for each dataset. For example, the third Eta EOF (Fig. 18, right) most likely corresponds to the second QuikSCAT vector EOF taken with the negative sign (Fig. 15, center).

The variance explained by the modes at any particular location differs greatly along the Pacific coast (Fig. 18). The Oregon and California coastal regions appear to be dominated by different wind stress regimes: the northern regime is effectively expressed in the first EOF mode, and the southern regime is reflected in the second mode. Although upwelling conditions characterize both the Oregon and California coastal regions during the summer, wind stress variability in these regions is spatially independent. A possible explanation is that the Oregon coast north of Cape Blanco is mainly influenced by changes in the location of the east Pacific high, while the California coast south of Cape Mendocino is influenced more by the development of the continental thermal low. Between Cape Blanco and Cape Mendocino, the wind stress variability has spatial structure associated with wind intensification around the capes, but temporally correlated with the alongshore winds in the northern regime. The region between Cape Blanco and Cape Mendocino effectively belongs to the northern regime.

It is of interest to compare this analysis with that of Kelly (1985), in which the first two EOFs had nearly uniform, alongshore wind fluctuations along the entire
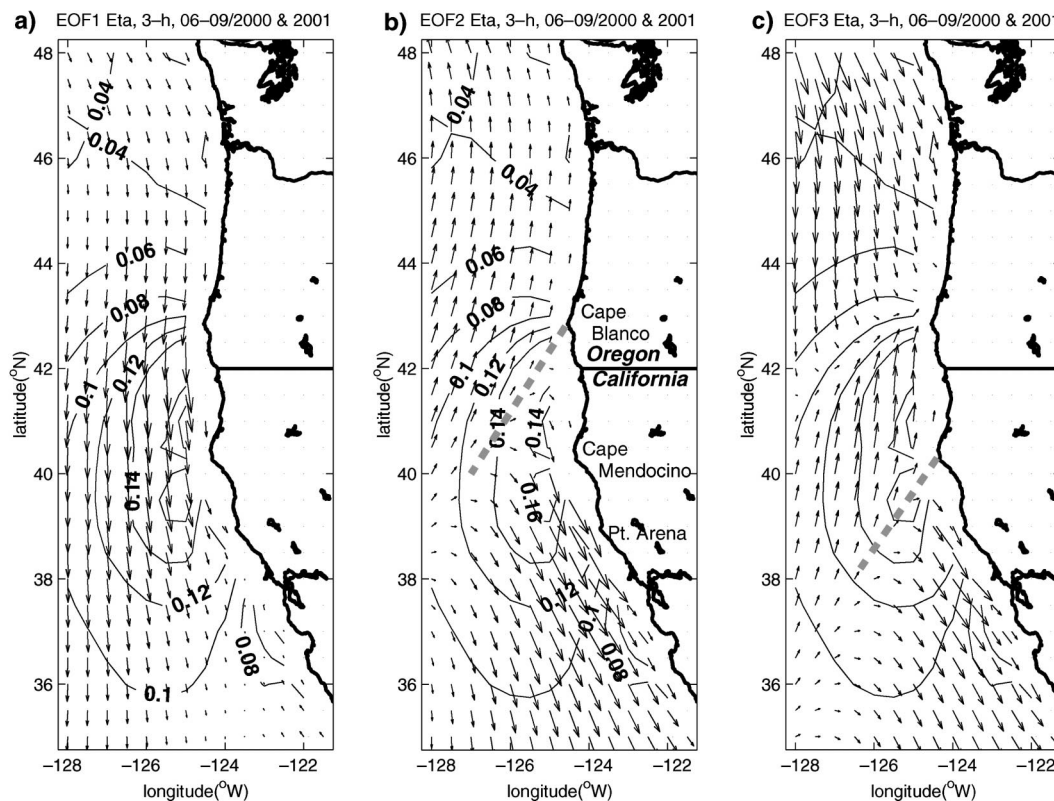
FIG. 17. (a)–(c) First three vector EOF modes of the Eta wind stress overlaid by the contours of the mean wind stress vector magnitude (N m^{-2}). All the available model 3-h archived wind fields during the two-summer period were used to compute the EOFs.

California coastal region between San Francisco and Point Conception. In her study, the spatial extent was limited to several coastal observational sites between Crescent City ($\approx$42°N) and Point Conception. Inclusion of the large area off Oregon and northern California in the present study leads to a different conclusion; the first two EOFs of the wind stress in Kelly's work correspond to the second and third functions resulted from Eta output. The leading EOF over the extended domain considered here is thus dominated by the energetic variability north of Cape Mendocino.

7. Wind stress curl and continental shelf winds

At frequencies lower than roughly 1 cpd, the wind stress (τ^x, τ^y) drives lateral Ekman transport in the oceanic surface boundary layer, and the curl of the wind stress ($\partial\tau^y/\partial x - \partial\tau^x/\partial y$) is proportional to the divergence of the oceanic Ekman transport (on scales small enough that the β effect can be neglected). This divergence is balanced by vertical motion (Ekman pumping) that efficiently drives ocean circulation in the geostrophic interior. It is thus of interest for oceanographic purposes to examine the structure of the wind stress curl fields.

The large-scale distribution of the QuikSCAT mean wind stress curl (Fig. 19a) shows positive (cyclonic)

curl along the coastal boundaries, and a weak negative curl over most of the offshore region. This general pattern is qualitatively similar to earlier climatological estimates for the California Current System (CCS) and other eastern boundary current (EBC) upwelling regions (Nelson 1977; Bakun and Nelson 1991). The mean QuikSCAT curl fields (Fig. 19a) show features associated with the orographic intensifications near Cape Blanco and Cape Mendocino, including positive maxima inshore between 40.5°–42.0°N and between 38.5°–40.0°N, and negative maxima to the southwest of Cape Blanco and Cape Mendocino, next to the corresponding positive inshore maxima. The spatial extent of these features is restricted to less than few tens of kilometers, with the absolute values of anticyclonic curl exceeding 10^{-6} N m^{-3}, several times larger than the weaker anticyclonic curl farther offshore. Similar, but smaller-scale features near Point Arena studied by Winant et al. (1988), and Enriquez and Friehe (1995), are not resolved by the 25-km QuikSCAT data or the models.

Mean wind stress curl fields derived from Eta Model (Fig. 19b) also show maxima downstream and offshore from the capes, but with maximum values smaller than for QuikSCAT. The Eta wind stress curl field is much smoother than the QuikSCAT curl field, and the anticyclonic wind stress curl features associated with the
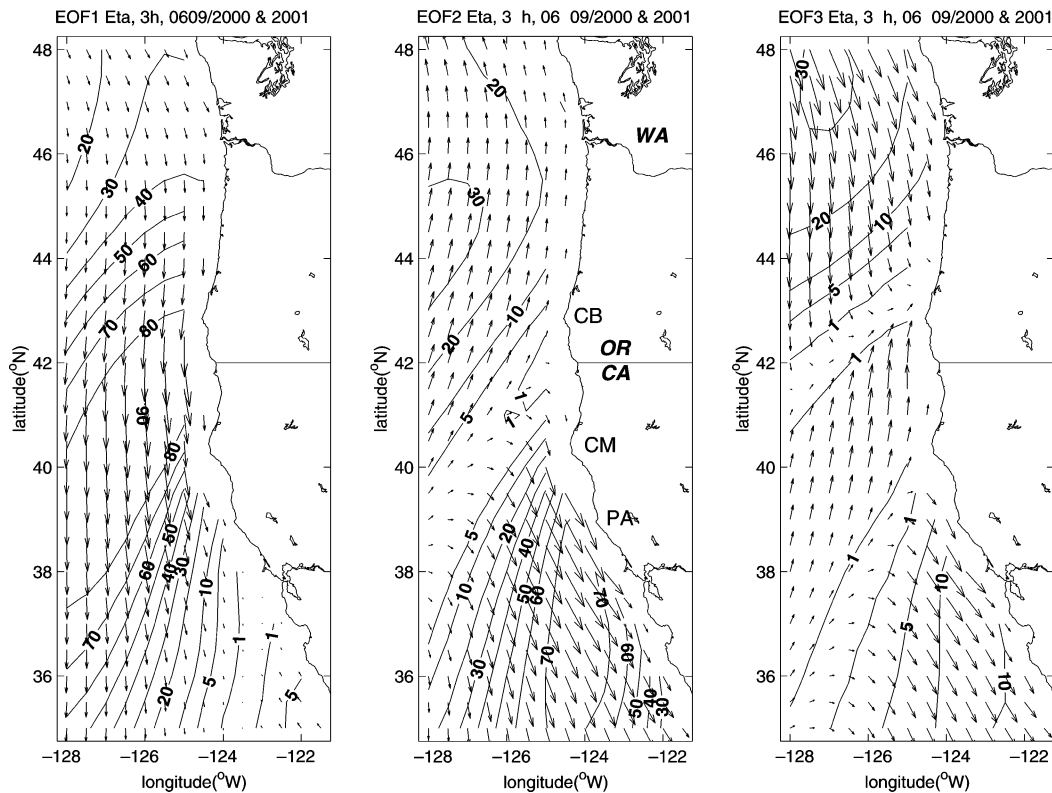
FIG. 18. Vectors are the same as in Fig. 17, overlaid by the contours of modal contributions into the local variance. Contours are 1%, 5%, and multiples of 10%.

capes are not reproduced in detail by the Eta Model. The finer resolution of the HR1 model allowed wind stress curl estimates closer to the coastal boundary. The resulting values of the cyclonic curl very near the coast were higher, peaking over 10^{-5} N m^{-3} adjacent to the coast south of Cape Blanco (Fig. 20). A maximum of the anticyclonic curl occurred offshore, between about 45° and 45.5°N, with values similar to QuikSCAT, but located closer to the coast. Along the central Oregon coast, from 45.5°N south to Cape Blanco, HR1 shows alternating bands of cyclonic and anticyclonic curl. These bands have roughly 50-km width, with the high values of positive curl adjacent to the coast, which then change sign offshore to negative, then to weak positive, and finally to weak negative that extends farther offshore. The intense positive curl adjacent to the coast may be influenced by the combination of high surface drag over land and large horizontal diffusion near the model grid scale.

In the CCS it is interesting to note that Cape Blanco appears to be the northernmost location where upwelling jets separate from the coast (Barth and Smith 1998; Barth et al. 2000); tongues of cold water extending seaward 100 m from the coast have also been found farther to the south in satellite images and drifter data (Ikeda and Emery 1984; Thomson and Papadakis 1987; Strub

et al. 1991). Samelson et al. (2002) suggest that Ekman pumping from local wind stress variations may contribute to this separation near Cape Blanco. Related observational and process-oriented modeling studies over other EBC region (Fiúza and Sousa 1989; McClain et al. 1986; Batteen et al. 1992) support the hypothesis that complex wind forcing can be an important driving mechanism for anticyclonic eddies, upwelling filaments, and cold water plumes. This complex wind forcing includes the combined effect of the anticyclonic wind stress curl and upwelling-favorable winds, as well as suggested "band forcing" along the coast (alternating bands of positive and negative wind stress curl). The present results a suggest similar hypothesis of a wind-driven mechanism for cold water plumes and anticyclonic eddy formation farther south in the CCS as well. Numerical modeling studies of the ocean response to spatially variable wind stress along the Oregon coast are in progress (Gan et al. 2004). In a recent related study based on similar model estimates of wind stress, Pickett and Paduan (2003) present evidence that offshore Ekman upwelling from wind stress curl is comparable to coastal Ekman transport divergence in the CCS region. Our results (Fig. 19) suggest that this offshore upwelling is generally confined within 100 km of the coast north of 38°N.
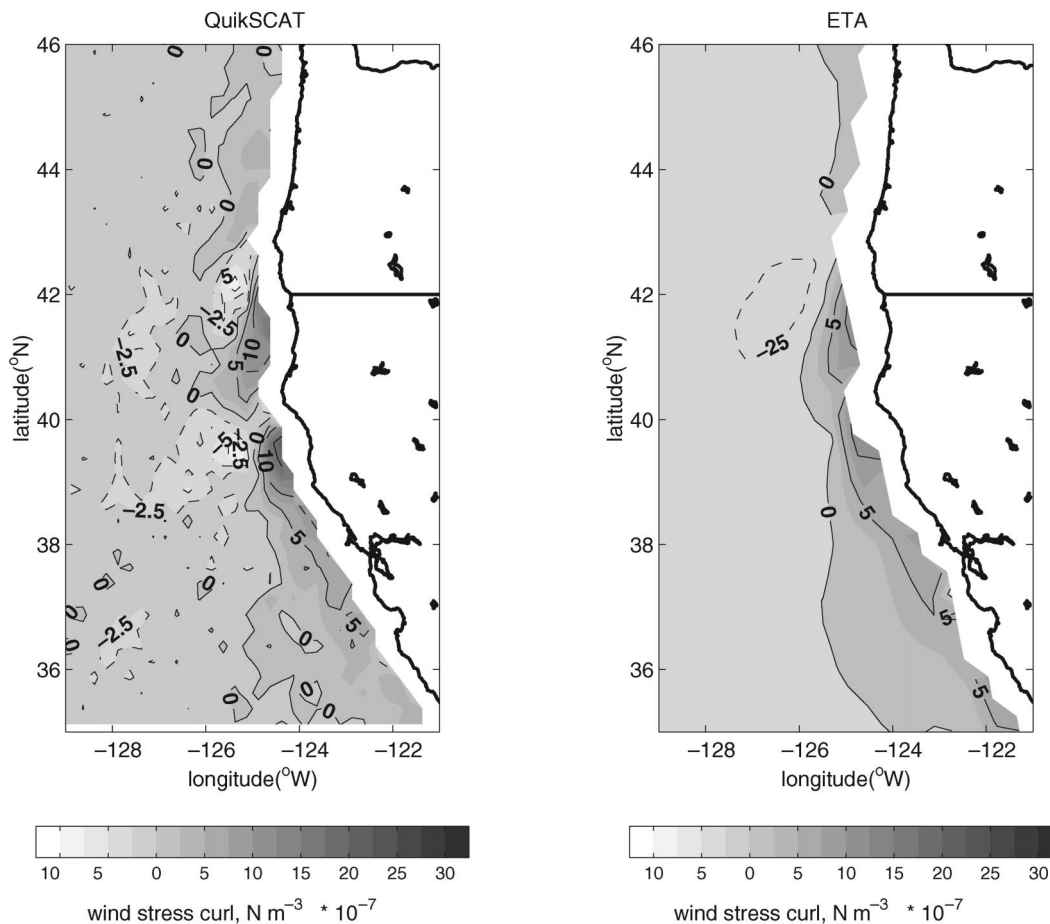
FIG. 19. Mean wind stress curl (N m^{-3} × 10^{-7}), Jun–Sep 2000 and 2001: (left) QuikSCAT and (right) Eta. Gray shading intervals are 2.5; negative contours (dashed lines) are 2.5 apart, positive contours are 5, 10, 20, 30, 70. QuikSCAT curl was computed from the wind stress by central differencing, and defined in the center of the regular 0.25° lat–lon grid. Eta wind stress curl was computed in the center of the model grid box, as a momentum flux through the given grid box area (irregular lat–lon grid).

8. Summary

In this study, the structure and dynamics of the surface wind fields in the coastal region extending offshore from Oregon and California to 130°W were examined during two summer periods, June through September 2000 and 2001. QuikSCAT satellite scatterometer measurements of surface wind stress were analyzed and compared with wind stresses from an operational mesoscale model (Eta) and two nested high-resolution mesoscale models centered on the Oregon coastal zone.

The mean summer wind stress had a southward component over the entire region in both years. Orographic intensifications of both the mean and fluctuating wind stress occurred near Cape Blanco, Cape Mendocino, and Point Arena. Wind stress curl computed from QuikSCAT and the models had complex structure, including intensive cyclonic and anticyclonic maxima associated with the orographic wind intensifications around the capes. The spatial scales of these orographic features, and the associated characteristic scales of the ocean up-

welling response along the continental shelf and slope are probably shorter than can be resolved by the 25-km footprint of the QuikSCAT data and by the model grid resolution of the order of tens of kilometers. The present results are generally consistent with the Samelson et al. (2002) hypothesis of a wind-driven influence on coastal jet separation near Cape Blanco.

Peak-to-peak mean diurnal fluctuations in wind stress, estimated from differences of twice-daily scatterometer measurements, were greater than 0.02 N m^{-2} over a broad region extending offshore up to 150 km, with maximum values exceeding 0.05 N m^{-2} near the coast. The sense of the diurnal cycle reversed near 41.5°N, with diurnal southward stress largest in the evening to the north and in the morning to the south, except near the regions of orographic intensification, where the southward stress adjacent to the coast was always largest in the evening.

Substantial differences between the model products were found for the mean, variable, and diurnal wind
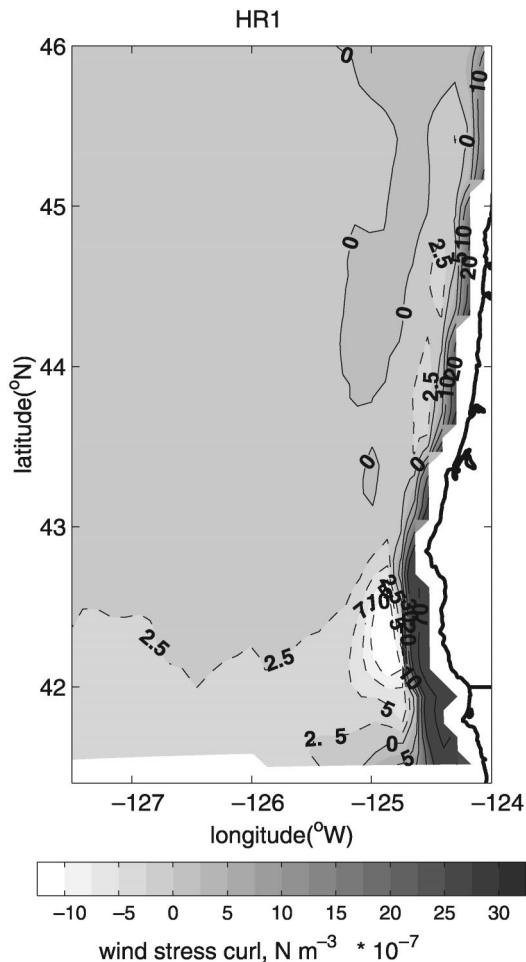
FIG. 20. Mean wind stress curl (N m^{-3} × 10^{-7}) along OR coast, Jun–Sep 2000 and 2001, from HR1 model. The calculations were done similarly to Eta, shown in Fig. 19b. Positive contours are 10, 20, 30, 70. There are 10 alongshore points with values over 10^{-5} N m^{-3}, and 10 points with values less than −10^{-6} N m^{-3}.

dependence with the wind stress variability off central and southern California. The southern wind stress regime corresponds to the enhanced upwelling-favorable wind stress along the California coast relative to the Oregon coast. The region between Cape Blanco and Cape Mendocino, where the wind stress variability depends predominately upon the wind intensification around the capes, effectively belongs to the northern regime. These northern and southern regimes may be separately controlled by the location and intensity of the east Pacific high and continental thermal low, respectively.

Many important questions remain concerning coastal wind fields. The amplitude of interannual variability in mean and fluctuating stress is not well known. The structure of the wind and wind stress fields within roughly 25 km of the coast, a region of particular oceanographic interest where diurnal and orographic effects are often large, is also poorly known. Models show some potential to reproduce some of these effects, but QuikSCAT observations are presently limited to the region beyond about 30 km from the coast. Preliminary analyses (M. Freilich 2004, personal communication) suggest that improved processing techniques may allow significantly higher-resolution (perhaps better than 10 km) wind stress estimates from existing satellite scatterometers.

stress fields. Model wind fields were more similar to each other than were the model stress fields. Differences between the observed and modeled stress fields near Cape Blanco were found to result in large differences in the estimates of local wind stress curl, with corresponding important implications for ocean modeling. Temporal correlations with the QuikSCAT observations are highest for the operational model, and are not improved by either nested high-resolution model. The highest-resolution nested model reproduced most accurately the mean observed stress fields, but slightly degraded the temporal correlations due to incoherent high-frequency (0.5–2 cpd) fluctuations.

EOF analysis indicated that the Oregon and California coastal regions appear to be dominated by different wind stress regimes. The northern regime corresponds to alongshore upwelling-favorable winds fluctuations off the Oregon coast, with an amplified effect downwind and offshore of Cape Blanco, and little or no spatial

REFERENCES

Bakun, A., and C. S. Nelson, 1991: Wind stress curl in subtropical eastern boundary current regions. *J. Phys. Oceanogr.,* **21,** 1815–1834.

Barth, J. A., and R. L. Smith, 1998: Separation of a coastal upwelling jet at Cape Blanco, Oregon, USA. *Benguela Dyn. South African J. Mar. Sci.,* **19,** 5–14.

——, S. D. Pierse, and R. L. Smith, 2000: A separating coastal upwelling jet at Cape Blanco, Oregon, and its connection to the California Current System. *Deep-Sea Res.,* **47B,** 783–810.

Batteen, M. L., C. N. L. da Costa, and C. S. Nelson, 1992: A numerical study of wind stress curl effects on eddies and filaments off the northwest coast of the Iberian Peninsula. *J. Mar. Syst.,* **3,** 249–266.

Beardsley, R. C., C. E. Dorman, C. A. Friehe, L. K. Rosenfeld, and C. D. Winant, 1987: Local atmospheric forcing during the Coastal Ocean Dynamics Experiment. 1. A description of the marine boundary layer and atmospheric conditions over a northern California upwelling region. *J. Geophys. Res.,* **92,** 1467–1488.

Bielli, S., P. L. Barbour, R. M. Samelson, E. Skyllingstad, and J. Wilczak, 2002: Numerical study of the diurnal cycle along the central Oregon coast during summertime northerly flow. *Mon. Wea. Rev.,* **130,** 992–1008.

Black, T. L., 1994: The new NMC mesoscale Eta Model: Description and forecast examples. *Wea. Forecasting,* **9,** 265–278.

Burk, S. D., and W. T. Thompson, 1996: The summertime low-level jet and marine boundary layer structure along the California coast. *Mon. Wea. Rev.,* **124,** 668–686.

——, T. Haack, and R. M. Samelson, 1999: Mesoscale simulation of supercritical, subcritical, and transcritical flow along coastal topography. *J. Atmos. Sci.,* **56,** 2780–2795.

Cleveland, W. S., 1979: Robust locally weighted regression and smoothing scatterplots. *J. Amer. Stat. Assoc.,* **74,** 829–836.

Crosby, D. S., L. C. Breaker, and W. H. Gemmill, 1993: A proposed definition for vector correlation in geophysics: Theory and application. *J. Atmos. Oceanic Technol.,* **10,** 355–367.

Deardorff, J. W., 1980: Stratocumulus-capped mixed layers derived from a three-dimensional model. *Bound.-Layer Meteor.,* **18,** 495–527.

Dorman, C. E., T. Holt, D. P. Rogers, and K. A. Edwards, 2000: Large-scale structure of the June–July 1996 marine atmospheric boundary layer along California and Oregon. *Mon. Wea. Rev.,* **128,** 1632–1652.

Edwards, K. A., A. M. Rogerson, C. D. Winant, and D. P. Rogers, 2001: Adjustment of the marine atmospheric boundary layer to a coastal cape. *J. Atmos. Sci.,* **58,** 1511–1528.

——, C. E. Dorman, and D. P. Rogers, 2002: Adjustment of the marine atmosphere boundary layer to the large-scale bend in the California coast. *J. Geophys. Res.,* **107,** 3213, doi:10.1029/2001JC000807.

Elliott, D. L., and J. J. O'Brien, 1977: Observational studies of the marine boundary layer over an upwelling region. *Mon. Wea. Rev.,* **105,** 86–98.

Enriquez, A. G., and C. A. Friehe, 1995: Effects of wind stress and wind stress curl variability on coastal upwelling. *J. Phys. Oceanogr.,* **25,** 1651–1671.

Fairall, C. W., E. F. Bradley, D. P. Rogers, J. B. Edson, and G. S. Young, 1996: Bulk parameterization of air-sea fluxes for Tropical Ocean-Global Atmosphere Coupled Ocean–Atmosphere Response Experiment. *J. Geophys. Res.,* **101,** 3747–3764.

Fiúza, A. F. G., and F. M. Sousa, 1989: Preliminary results of a CTD survey in the Coastal Transition Zone off Portugal during 1–9 September 1988. *Coastal Transition Zone Newsl.,* **4,** 2–9.

Fleagle, R. W., and J. A. Businger, 1980: *An Introduction to Atmospheric Physics.* Academic Press, 432 pp.

Freilich, M. H., and R. S. Dunbar, 1999: The accuracy of the NSCAT 1 vector winds: Comparisons with National Data Buoy Center buoys. *J. Geophys. Res.,* **104** (C5), 11 231–11 246.

Gan, J., J. S. Allen, and R. M. Samelson, 2004: On open boundary conditions for a limited-area coastal model off Oregon. Part 2: Response to wind forcing from a regional mesoscale atmospheric model. *Ocean Modell.,* in press.

Gille, S. T., S. G. Llewellyn Smith, and S. M. Lee, 2003: Measuring the sea breeze from QuikSCAT Scatterometry. *Geophys. Res. Lett.,* **30,** 1114, doi:10.1029/2002GL016320.

Halliwell, G. R., and J. S. Allen, 1987: The large-scale coastal wind field along the west coast of North America, 1981–1982. *J. Geophys. Res.,* **92** (C2), 1861–1884.

Halpern, D., 1976: Structure of a coastal upwelling event observed off Oregon during July 1973. *Deep-Sea Res.,* **23,** 495–508.

Hodur, R. M., 1997: The Naval Research Laboratory's Coupled Ocean/Atmosphere Mesoscale Prediction System (COAMPS). *Mon. Wea. Rev.,* **125,** 1414–1430.

Holt, T. R., 1996: Mesoscale forcing of a boundary layer jet along the California coast. *J. Geophys. Res.,* **101** (D2), 4235–4254.

Huyer, A., 1983: Coastal upwelling in the California current system. *Progress in Oceanography,* Vol. 12, Pergamon, 259–284.

Ikeda, M., and W. J. Emery, 1984: Satellite observations and modeling of meanders in the California Current System off Oregon and northern California. *J. Phys. Oceanogr.,* **14,** 1434–1450.

Janjić, Z. I., 1994: The step-mountain eta coordinate model: Further developments of the convection, viscous sublayer, and turbulence closure schemes. *Mon. Wea. Rev.,* **122,** 927–945.

Kelly, K. A., 1985: The influence of winds and topography on the sea surface temperature patterns over the northern California slope. *J. Geophys. Res.,* **90** (C6), 11 783–11 798.

Koracin, D., and C. E. Dorman, 2001: Marine atmospheric boundary layer divergence and clouds along California in June 1996. *Mon. Wea. Rev.,* **129,** 2040–2056.

Kundu, P. K., 1976: Ekman veering observed near the ocean bottom. *J. Phys. Oceanogr.,* **6,** 238–242.

Large, W. G., and S. Pond, 1982: Sensible and latent heat flux measurements over the ocean. *J. Phys. Oceanogr.,* **12,** 464–482.

Lerczak, J. A., M. C. Hendershott, and C. D. Winant, 2001: Observations and modeling of coastal internal waves driven by a diurnal sea breeze. *J. Geophys. Res.,* **106** (C9), 19 715–19 730.

Liu, W. T., 2002: Progress in scatterometer application. *J. Oceanogr.,* **58,** 121–136.

——, and W. Tang, 1996: Equivalent neutral wind. JPL Publ. 96-17, Jet Propulsion Laboratory, Pasadena, CA, 16 pp.

——, and X. Xie, 2001: Improvement in spacebased scatterometers and increased scientific impact in the past decade. *Proc. Oceans 2001,* Honolulu, HI, Vol. 1, Marine Technology Society, 626–630.

Lobocki, L., 1993: A procedure for the derivation of surface-layer bulk relationships from simplified second-order closure models. *J. Appl. Meteor.,* **32,** 126–138.

Louis, J.-F., 1979: A parametric model of vertical eddy fluxes in the atmosphere. *Bound.-Layer Meteor.,* **17,** 187–202.

McClain, C. R., Sh.-Y. Chao, L. P. Atkinson, J. O. Blanton, and F. de Castillejo, 1986: Wind-driven upwelling in the vicinity of Cape Finisterre, Spain. *J. Geophys. Res.,* **91** (C7), 8470–8486.

Mellor, G. L., and T. Yamada, 1982: Development of a turbulence closure model for geophysical fluid problems. *Rev. Geophys. Space Phys.,* **20,** 851–875.

Mittelstadt, J., cited 1998: The Eta-32 model. Western Region Tech. Attachment 98-03. [Available online at http://www.wrh.noaa.gov/wrhq/98TAs/9803/index.html.]

Moeng, C.-H., 1984: A large-eddy-simulation model for the study of planetary boundary-layer turbulence. *J. Atmos. Sci.,* **41,** 2052–2062.

Naderi, F. M., M. H. Freilich, and D. G. Long, 1991: Spaceborne radar measurement of wind velocity over the ocean: An overview of the NSCAT scatterometer system. *Proc. IEEE,* **79,** 850–866.

Nelson, C. S., 1977: Wind stress and wind stress curl over the California Current. NOAA Tech. Rep. 714, 87 pp.

Pickett, M. H., and J. D. Paduan, 2003: Ekman transport and pumping in the California Current based on the U.S. Navy's high-resolution atmospheric model (COAMPS). *J. Geophys. Res.,* **108,** 3327, doi:10.1029/2003JC001902.

Rogerson, A. M., 1999: Transcritical flow in the coastal marine atmospheric boundary layer. *J. Atmos. Sci.,* **56,** 2761–2779.

Samelson, R. M., 1992: Supercritical marine layer flow along a smoothly varying coastline. *J. Atmos. Sci.,* **49,** 1571–1584.

——, and S. J. Lentz, 1994: The horizontal momentum balance in the marine atmospheric boundary layer during CODE-2. *J. Atmos. Sci.,* **51,** 3745–3757.

——, and Coauthors, 2002: Wind stress forcing of the Oregon coastal ocean during the 1999 upwelling season. *J. Geophys. Res.,* **107,** 3034, doi:10.1029/2001JC000900.

Schlax, M. G., and D. B. Chelton, 1992: Frequency domain diagnostics for linear smoothers. *J. Amer. Stat. Assoc.,* **87,** 1070–1081.

Smith, R. L., 1974: A description of current, wind, and sea level variations during coastal upwelling off the Oregon coast, July–August 1972. *J. Geophys. Res.,* **79,** 435–443.

Staudenmaier, M., cited 1996: A description of the Meso Eta model. Western Region Tech. Attachment 96-06. [Available online at http://www/wrh.noaa.gov/wrhq/96TAs/TA9606/ta96-06.html.]

Strub, P. T., P. M. Kosro, and A. Huyer, 1991: The nature of the cold filaments in the California Current system. *J. Geophys. Res.,* **96** (C8), 14 743–14 768.

Sun, W.-Y., and C.-Z. Chang, 1986: Diffusion model for a convective

layer. Part I: Numerical simulation of convective boundary layer. *J. Climate Appl. Meteor.,* **25,** 1445–1453.

Thomson, R. E., and J. E. Papadakis, 1987: Upwelling filaments and motion of a satellite-tracked drifter along the west coast of North America. *J. Geophys. Res.,* **92** (C6), 6445–6461.

Winant, C. D., C. E. Dorman, C. A. Friehe, and R. C. Beardsley, 1988: The marine layer off northern California: An example of supercritical channel flow. *J. Atmos. Sci.,* **45,** 3588–3605.

Xue, M., K. K. Droegemeier, V. Wong, A. Shapiro, and K. Brewster, 1995: ARPS Version 4.0 user's guide. ARPS, Center for Analysis and Prediction of Storms, 380 pp. [Available from Center for Analysis and Prediction of Storms, University of Oklahoma, Norman, OK 73072.]

Zemba, J., and C. A. Friehe, 1987: The marine atmospheric boundary layer jet in the Coastal Ocean Dynamics Experiment. *J. Geophys. Res.,* **92,** 1489–1496.